


Optimal performance of voltage-probe quantum heat engines

Zahra Sartipi¹ and Javad Vahedi^{2,1,*}

¹*Department of Physics, Sari Branch, Islamic Azad University, Sari 48164-194, Iran*

²*Kirchhoff-Institut für Physik, Universität Heidelberg, Im Neuenheimer Feld 227, 69120 Heidelberg, Germany*

 (Received 1 May 2023; revised 24 October 2023; accepted 8 November 2023; published 27 November 2023)

The thermoelectric performance at a given output power of a voltage-probe heat engine, exposed to an external magnetic field, is investigated in linear irreversible thermodynamics. For the model, asymmetric parameter, general figures of merit, and efficiency at a given output power are analytically derived. Results show a tradeoff between efficiency and output power, and we recognize optimum-efficiency values at a given output power are enhanced compared to a Büttiker-probe heat engine due to the presence of a characteristic parameter, namely, d_m . Moreover, similar to a Büttiker-probe heat engine, the universal bounds on the efficiency are obtained, and the efficiency at a given output power can exceed the Curzon-Ahlborn limit. These findings have practical implications for the optimization of realistic heat engines and refrigerators. By controlling the values of the asymmetric parameter, the figures of merit, and d_m , it may be possible to design more efficient and powerful thermoelectric devices.

DOI: [10.1103/PhysRevB.108.195435](https://doi.org/10.1103/PhysRevB.108.195435)

I. INTRODUCTION

The thermoelectric performance of quantum heat engines is an attractive field of interest for researchers from the experimental and theoretical communities. This is due to advances in material science and the constant demand for more advanced and powerful energy harvesting [1–9]. Nevertheless, the efficiency of heat engines is restricted from above by the efficiency of Carnot heat engines. Therefore, fabricating heat engines with high performance is highly demanded.

It is well known that ideal heat engines working under reversible processes lack practical function due to their zero output power. Accordingly, finite-time thermodynamics was invented to optimize the thermoelectric performance of heat devices [10–15]. Moreover, macroscopic or quantum heat engines should not operate in the maximum output power region due to the relatively small efficiency, and thermal machines with higher efficiency can be achieved in a regime with smaller output power. Whitney [16] showed that maximum efficiency for quantum heat engines can be obtained somewhere close to the maximum output power. Holubec and Ryabov [17–19] reported on the optimal performance of irreversible and low-dissipation heat engines. Based on their work, quantum heat engines performing near maximum output power can offer significantly higher efficiency than the maximum output power efficiency. Long *et al.* [20] investigated the efficiency of minimally nonlinear irreversible quantum heat engines at a given output power. This gave additional insight into efficiency since the output power of actual heat engines is below the maximum output power.

The optimization of real thermoelectric devices at a given power is of significant current interest due to the

above-mentioned points. In this context exposing heat engines to an external magnetic field introduces complexity by breaking time-reversal symmetry in the system. Based on the work of Benenti *et al.* [21], in any heat engine with broken time-reversal symmetry, both maximum efficiency and maximum output power efficiency are described by an asymmetry parameter and a general figure of merit. This could lead to an efficiency enhancement of the heat engine in the linear response regime. While the exact details of this process are still being studied and optimized [22,23], the idea of using external magnetic fields to enhance the efficiency of quantum heat engines is an active area of research with promising results [24–27].

In this context, adding more terminals to the heat engines also opens up the path to achieving higher efficiency and unveiling novel phenomena [28,29]. Multiterminal heat engines offer several advantages over traditional two-terminal heat engines [30–37]. For example, they can potentially achieve higher efficiency by allowing for more complex and efficient heat exchange between the engine and the external environment [38–40]. They can also exhibit novel thermodynamic phenomena that are not present in two-terminal heat engines. For instance, it might be possible for these complex systems to decouple charge and energy flows, leading to higher thermoelectric properties [41–44].

For a multiterminal device with an external magnetic field, due to the broken time-reversal symmetry, a new bound on the Onsager coefficients has been achieved within the framework of linear irreversible thermodynamics, offering a unique insight into the optimal performance of a heat engine [32–35]. Zhang *et al.* [45] addressed how an external magnetic field could enhance the thermoelectric properties of a three-terminal quantum heat engine with a Büttiker probe at a given output power. They demonstrated that broken time-reversal symmetry gives rise to a broad region of parameters

*javahedi@kip.uni-heidelberg.de

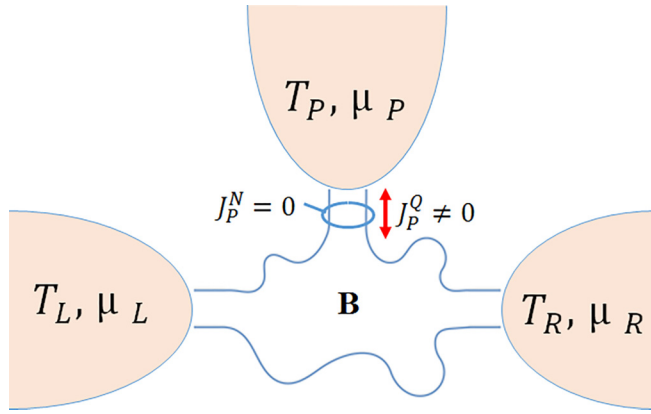


FIG. 1. Schematic drawing of a voltage-probe heat engine in the presence of an external magnetic field (\mathbf{B}).

for optimizing the performance of nanoscale heat engines. Furthermore, they obtained a different universal bound on the efficiency at a given output power of the quantum heat engine with broken time-reversal symmetry. In another work, Lu *et al.* [46] examined the thermoelectric properties of a three-terminal thermoelectric engines with two independent output electric currents and one input heat current. Based on their work, the heat engine with two output electric currents can significantly increase efficiency and output power.

Despite the studies mentioned above, the performance optimization of a voltage-probe quantum heat engine [12,47,48], with broken time-reversal symmetry, has not been investigated yet. This study aims to fill this gap by comparing the efficiencies of voltage-probe and Büttiker-probe heat engines operating at a given output power within the linear response regime and broken time-reversal symmetry. In this regard, it is worth noting that the most closely related previous work is that of Zhang *et al.* [45] who investigated a three-terminal setup in the presence of an external magnetic field within the context of Büttiker probe. The primary difference between a voltage probe and a Büttiker probe lies in how they are adjusted to exchange particle and heat current with the scattering region. The voltage probe (see Fig. 1) allows energy (heat) to be exchanged while no net charge flow. The Büttiker probe, on the other hand, is designed to be in equilibrium, blocking the transfer of particle and heat currents with the scattering region, serving as a phase-randomizing agent. A significant benefit of utilizing such probes lies in their ability to effectively mimic inelastic scattering phenomena in a phenomenological way [49]. The Landauer scattering approach suffers from the fact that it focuses on purely coherent quantum transport. In reality, systems often show only partial coherence due to the inelastic scattering processes, including interactions between electrons and other particles such as phonons, photons, and other electrons. By adding probe reservoirs into the model, one can simulate these inelastic scattering events. A major advantage of this methodology is its straightforwardness and its ability to mimic the behavior of inelastic scattering without having to address the microscopic details.

We introduce different parameters: the normalized efficiency [$\eta_m/\eta_m(\mathcal{P}_{\max})$], the asymmetric parameter (x_m), the

general figure of merit (y_m), and an additional unique parameter (d_m). These parameters are categorized into three scenarios, $m = L$, $m = P$, and $m = LP$, corresponding to reservoir(s) L , P , and both L and P , from which heat current is extracted and absorbed by the scattering region in each cycle, respectively. Our results illustrate that the voltage-probe heat engine, because of the key parameter d_m , can adjust the upper bound on the general figure of merit y_m , in contrast with a Büttiker-probe setup. This means that the efficiency value at a given output power is controlled by d_m , and the optimum-efficiency value increases for $d_m < 1$.

The rest of the paper is organized as follows. In Sec. II, we elaborate on the efficiency properties at a given output power of voltage-probe quantum heat engines with an external magnetic field and show mathematically under which condition the voltage-probe heat engine is converted into the Büttiker-probe one. We present our main results in Sec. III. Conclusions are summarized in Sec. IV. In Appendixes A–E, all detailed of calculations are presented.

II. MODEL AND METHOD

A. General setup

The voltage-probe setup illustrated in Fig. 1 contains a scattering region in contact with electronic reservoirs with temperatures and chemical potentials, described as $T_\alpha = T + \Delta T_\alpha$ and $\mu_\alpha = \mu + \Delta\mu_\alpha$, where $\alpha = L, P, R$ denotes respective reservoirs. Inelastic scattering phenomena [12] are simulated using a voltage probe whose temperature and chemical-potential parameters are adjusted to block particle current ($J_P^N = 0$) while allowing heat current ($J_P^Q \neq 0$). We assume the right reservoir (R) as a reference so that $\mu_R = \mu$ and $T_R = T$. The setup is also designed to work in the linear response regime with $|\Delta\mu_\alpha|/k_B T \ll 1$ and $|\Delta T_\alpha|/T \ll 1$, where k_B is the Boltzmann constant. Energy (J_α^U) and particle (J_α^N) currents flowing from the α th reservoir into the scattering region satisfy the current conservation law by the constraint $\sum_\alpha J_\alpha^{U(N)} = 0$, where $\alpha = L, R, P$. Heat current J_α^Q is related to the J_α^U and J_α^N by $J_\alpha^Q = J_\alpha^U - eV_\alpha J_\alpha^N$, where $V_\alpha = \mu_\alpha/e$ is the reservoir voltage. Charge current is directly proportional to the particle current by $J_\alpha^e = eJ_\alpha^N$, where e is the electron charge. Note that the positive current values are associated with flows from the respective reservoirs to the scattering region. Using the Landauer-Büttiker formalism, it is possible to derive the coherent flow of heat J_α^Q and particles J_α^N via a noninteracting conductor (see Appendix A for more details).

The relation $\dot{S} = \sum_\alpha J_\alpha^Q/T_\alpha$ gives the sum of the entropy production rate, and within the linear response regime, it can be described as $\dot{S} = JX = \sum_{\alpha=1}^4 J_\alpha X_\alpha$, where J and X are four-dimensional vectors defined as follows:

$$\begin{aligned} J &= (J_L^N, J_L^Q, J_P^N, J_P^Q), \\ X &= (X_L^V, X_L^T, X_P^V, X_P^T), \end{aligned} \quad (1)$$

where $X_\alpha^V = \Delta V_\alpha/T$ and $X_\alpha^T = \Delta T_\alpha/T^2$ ($\alpha = L, P$) are the generalized forces. Assuming that the thermodynamic forces are small in the linear response regime, the relationship between generalized forces X_α (driving irreversible processes) and fluxes J_α (the system's response to the external forces) is

linear so that

$$J = \mathcal{L}X, \quad (2)$$

where \mathcal{L} is a 4×4 Onsager matrix. Equation (2) can be recast in a matrix form as follows:

$$\begin{bmatrix} J_L^N \\ J_L^Q \\ J_P^N \\ J_P^Q \end{bmatrix} = \begin{bmatrix} \mathcal{L}_{11} & \mathcal{L}_{12} & \mathcal{L}_{13} & \mathcal{L}_{14} \\ \mathcal{L}_{21} & \mathcal{L}_{22} & \mathcal{L}_{23} & \mathcal{L}_{24} \\ \mathcal{L}_{31} & \mathcal{L}_{32} & \mathcal{L}_{33} & \mathcal{L}_{34} \\ \mathcal{L}_{41} & \mathcal{L}_{42} & \mathcal{L}_{43} & \mathcal{L}_{44} \end{bmatrix} \begin{bmatrix} X_L^V \\ X_L^T \\ X_P^V \\ X_P^T \end{bmatrix}, \quad (3)$$

where \mathcal{L}_{ii} and \mathcal{L}_{ij} are diagonal and off-diagonal elements, respectively, which are given in Appendix B [see Eq. (B1)]. Since the probe reservoir neither releases particles nor absorbs ($J_P^N = 0$), the problem can reduce to threeparticle and heat fluxes that are related to the respective generalized forces by the Onsager matrix \mathcal{L}' as follows:

$$\begin{bmatrix} J_L^N \\ J_L^Q \\ J_P^Q \end{bmatrix} = \begin{bmatrix} \mathcal{L}'_{11} & \mathcal{L}'_{12} & \mathcal{L}'_{13} \\ \mathcal{L}'_{21} & \mathcal{L}'_{22} & \mathcal{L}'_{23} \\ \mathcal{L}'_{31} & \mathcal{L}'_{32} & \mathcal{L}'_{33} \end{bmatrix} \begin{bmatrix} X_L^V \\ X_L^T \\ X_P^T \end{bmatrix}, \quad (4)$$

where \mathcal{L}'_{ij} are expressed in Appendix B [see Eq. (B3)].

We notice that the Onsager matrix of the Büttiker-probe engine [45] can be retrieved from Eq. (4) by imposing $J_P^Q = 0$, which leads to the 2×2 Onsager matrix as follows:

$$\begin{bmatrix} J_L^N \\ J_L^Q \end{bmatrix} = \begin{bmatrix} \mathcal{L}''_{11} & \mathcal{L}''_{12} \\ \mathcal{L}''_{21} & \mathcal{L}''_{22} \end{bmatrix} \begin{bmatrix} X_L^V \\ X_L^T \end{bmatrix}, \quad (5)$$

where \mathcal{L}''_{ij} are given in Appendix B [see Eq. (B4)].

Now we expose the setup by an external magnetic field (\mathbf{B}). With the presence of a magnetic field (\mathbf{B}), the laws of physics remain constant if time t is replaced by $-t$, provided that the field \mathbf{B} is replaced by $-\mathbf{B}$. In this case, the Onsager-Casimir relations for the off-diagonal terms of the Onsager matrix are expressed as

$$\mathcal{L}_{ij}(\mathbf{B}) = \mathcal{L}_{ji}(-\mathbf{B}) \quad (6)$$

when \mathbf{B} vanishes, the Onsager reciprocal relation $\mathcal{L}_{ij} = \mathcal{L}_{ji}$ is retrieved.

B. Bounds on Onsager matrix

For a two-terminal heat engine, the second law of thermodynamics constrains the Onsager matrix coefficients, and it is derived from the positivity of the entropy production rate [21], namely, $\dot{S} \geq 0$. Nevertheless, for a three-terminal setup with $\mathbf{B} \neq 0$, current conservation is mathematically expressed by unitarity of the scattering matrix, imposing additional bounds on the Onsager matrix elements, more robust than those obtained from the positivity of entropy production rate [32,34]. Therefore, it requires to fulfill the following inequalities for a voltage-probe heat engine:

$$\begin{aligned} \mathfrak{L}_{11} &\geq 0, \\ \mathfrak{L}_{22} &\geq 0, \\ \mathfrak{L}_{11}\mathfrak{L}_{22} + \mathfrak{L}_{12}\mathfrak{L}_{21} - [\mathfrak{L}_{12}^2 - \mathfrak{L}_{21}^2] &\geq 0, \end{aligned} \quad (7)$$

where

$$\begin{aligned} \mathfrak{L}_{11} &= \mathcal{L}'_{11}(\mathbf{B}), \\ \mathfrak{L}_{12} &= \mathcal{L}'_{12}(\mathbf{B}) + \mathcal{L}'_{13}(\mathbf{B})\xi, \\ \mathfrak{L}_{21} &= \mathcal{L}'_{21}(\mathbf{B}) + \mathcal{L}'_{31}(\mathbf{B})\xi, \\ \mathfrak{L}_{22} &= \mathcal{L}'_{22}(\mathbf{B}) + \mathcal{L}'_{33}(\mathbf{B})\xi^2 + [\mathcal{L}'_{23}(\mathbf{B}) + \mathcal{L}'_{32}(\mathbf{B})]\xi, \end{aligned} \quad (8)$$

and $\xi = X_P^T/X_L^T$. In what follows, we will drop \mathbf{B} in the Onsager coefficients for simplicity. By setting the limit $J_P^Q = 0$, the inequalities for a Büttiker-probe heat engine can be achieved [34,35,45], so

$$\begin{aligned} \mathcal{L}''_{11} &\geq 0, \\ \mathcal{L}''_{22} &\geq 0, \\ \mathcal{L}''_{11}\mathcal{L}''_{22} + \mathcal{L}''_{12}\mathcal{L}''_{21} - [\mathcal{L}''_{12}^2 - \mathcal{L}''_{21}^2] &\geq 0, \end{aligned} \quad (9)$$

C. Transport coefficients

Onsager coefficients are linked to the transport coefficients, namely, the Seebeck coefficient (S_{ij}), electrical conductance (G_{ij}), thermal conductance (K_{ij}), and Peltier coefficient (Π_{ij}). Multiterminal thermoelectric devices introduce nonlocal transport coefficients with index $i \neq j$, describing how applied bias between two terminals influences transport properties in the remaining terminals [42].

For a multiterminal heat engine, S_{ij} is given by the relationship between potential and temperature biases between terminals, assuming no net particle current is flowing through the system [42]

$$S_{ij} = -\frac{\Delta V_i}{\Delta T_j} \Big|_{\substack{J_\alpha^N=0 \forall \alpha \\ \Delta T_\alpha=0 \forall \alpha \neq j}}, \quad (10)$$

and for a voltage-probe heat engine, it can be described as follows:

$$S_{LL}(\mathbf{B}) = \frac{\mathcal{L}'_{12}}{T\mathcal{L}'_{11}}, \quad S_{LP}(\mathbf{B}) = \frac{\mathcal{L}'_{13}}{T\mathcal{L}'_{11}}, \quad (11)$$

$$S_{LL}(-\mathbf{B}) = \frac{\mathcal{L}'_{21}}{T\mathcal{L}'_{11}}, \quad S_{LP}(-\mathbf{B}) = \frac{\mathcal{L}'_{31}}{T\mathcal{L}'_{11}}, \quad (12)$$

where S_{LL} and S_{LP} represent local and nonlocal coefficients, respectively. Using Eq. (5), we can derive the Seebeck coefficient for the Büttiker-probe heat engine as follows:

$$S_{LL}(\mathbf{B}) = \frac{\mathcal{L}''_{12}}{T\mathcal{L}''_{11}}, \quad S_{LL}(-\mathbf{B}) = \frac{\mathcal{L}''_{21}}{T\mathcal{L}''_{11}}. \quad (13)$$

The electrical conductance for the multiterminal setup generalizes to [42]

$$G_{ij} = \frac{J_i^N}{\Delta V_j} \Big|_{\substack{\Delta V_\alpha=0 \forall \alpha \neq j \\ \Delta T_\alpha=0 \forall \alpha}}, \quad (14)$$

and for a voltage-probe heat engine, it is given as

$$G_{LL} = \frac{\mathcal{L}'_{11}}{T}, \quad (15)$$

where G_{LL} denotes the local electrical coefficient. For the Büttiker-probe engine, it can be described as

$$G_{LL} = \frac{\mathcal{L}''_{11}}{T}. \quad (16)$$

The thermal conductance is expressed as [42]

$$K_{ij} = \frac{J_i^Q}{\Delta T_j \left(\sum_{\alpha=0 \forall \alpha}^{J_{\alpha}^N} \right)_{(\Delta T_{\alpha}=0 \forall \alpha \neq j)}}, \quad (17)$$

and for a voltage-probe engine, it can be written in terms of the Onsager coefficients with local K_{ii} and nonlocal K_{ij} coefficients as

$$K_{LL} = \frac{\mathcal{L}'_{22}\mathcal{L}'_{11} - \mathcal{L}'_{21}\mathcal{L}'_{12}}{T^2\mathcal{L}'_{11}}, \quad K_{PP} = \frac{\mathcal{L}'_{33}\mathcal{L}'_{11} - \mathcal{L}'_{31}\mathcal{L}'_{13}}{T^2\mathcal{L}'_{11}},$$

$$K_{LP} = \frac{\mathcal{L}'_{11}\mathcal{L}'_{23} - \mathcal{L}'_{21}\mathcal{L}'_{13}}{T^2\mathcal{L}'_{11}}, \quad K_{PL} = \frac{\mathcal{L}'_{11}\mathcal{L}'_{32} - \mathcal{L}'_{12}\mathcal{L}'_{31}}{T^2\mathcal{L}'_{11}}, \quad (18)$$

and for the Büttiker-probe heat engine, it gives

$$K_{LL} = \frac{\mathcal{L}''_{22}\mathcal{L}''_{11} - \mathcal{L}''_{21}\mathcal{L}''_{12}}{T^2\mathcal{L}''_{11}}. \quad (19)$$

In any thermoelectric device, the Peltier coefficient is related to the Seebeck coefficient as $\Pi_{ij}(\mathbf{B}) = TS_{ji}(-\mathbf{B})$ when $\mathbf{B} \neq 0$.

D. Thermodynamic efficiency of the steady-state heat engines

The efficiency of any steady-state heat engine is bounded from above by the Carnot-engine efficiency η_c , explained for a three-terminal heat engine in Appendix C. Given that a voltage-probe quantum heat engine is operating between three reservoirs at different temperatures T_L , T_P , and T_R , the efficiency is defined as [42]

$$\eta = \frac{\mathcal{P}}{\sum_{\alpha+} J_{\alpha}^Q} \leq \eta_c$$

$$= \frac{J_L^Q + J_P^Q + J_R^Q}{\sum_{\alpha+} J_{\alpha}^Q} = \frac{-T J_L^N X_L^V}{\sum_{\alpha+} J_{\alpha}^Q}, \quad (20)$$

where $\mathcal{P} > 0$ is the output power of the heat engine, equaling the sum of all heat exchanged between the scattering region and reservoirs, and the symbol $\sum_{\alpha+}$ in the denominator is only restricted to positive heat currents ($J_{\alpha}^Q > 0$, where $\alpha = L, P$). For the voltage-probe quantum heat engine sketched in Fig. 1, for simplicity, we set $T_L > T_P > T_R$ and consider only those situations where J_R^Q is supplied by the scattering region ($J_R^Q < 0$). It is worth mentioning that within the regime that $J_R^Q > 0$, the system effectively works like a refrigerator, absorbing heat from the coldest reservoir(s). Taking these assumptions, when both J_L^Q and J_P^Q are absorbed from the respected reservoirs, the efficiency reads as

$$\eta_{LP} = \frac{\mathcal{P}}{J_L^Q + J_P^Q}, \quad (21)$$

and when either J_L^Q or J_P^Q is extracted from the respected reservoir, efficiency reads as

$$\eta_{L,(P)} = \frac{\mathcal{P}}{J_{L,(P)}^Q}, \quad (22)$$

the subscript L in the denominator is replaced by P if the probe reservoir is the only one that releases heat into the scattering

region and two other reservoirs absorb heat from it. Since the signs of the heat currents flowing throughout the scattering region and reservoirs are not *a priori*; in other words, it depends upon the details of the system, the efficiency expression relies on the heat current(s), injected into the scattering region from the respective reservoir(s). Note that, in the formalism developed in the following we refer to the efficiency of the voltage probe as η_m , with subindex $m = L, P, LP$. This discriminates it from the efficiency of Büttiker probe we refer to it with η .

E. Efficiency at maximum output power

Here we formulate $\eta_m(\mathcal{P}_{\max})$ in the context of the irreversible heat engine, for the three-terminal voltage-probe setup. From Eq. (4), it can be found that the output power of a voltage-probe heat engine is a function of three generalized forces, namely, X_L^V , X_L^T , and X_P^T , and it can be written as

$$\mathcal{P} = -T(J_L^N X_L^V) > 0, \quad (23)$$

where $J_L^N = \mathcal{L}'_{11}X_L^V + (\mathcal{L}'_{12} + \mathcal{L}'_{13}\xi)X_L^T$. To derive the maximum output power of the heat engine, the derivative of \mathcal{P} with respect to X_L^V is calculated while X_L^T and X_P^T are kept constant, so

$$X_L^{V*} = \frac{-\mathcal{L}_{12}}{2\mathcal{L}_{11}}X_L^T. \quad (24)$$

Inserting X_L^{V*} into Eq. (23), the maximum output power can be defined as

$$\mathcal{P}_{\max} = \frac{T^4}{4}\mathbb{G}\mathbb{S}^2X_L^{T2}, \quad (25)$$

where $\mathbb{G} = G_{LL}$ and $\mathbb{S} = (S_{LL} + S_{LP}\xi)$. Exploiting Eqs. (24) and (25), efficiency at maximum output power for different cases detailed in Eqs. (21) and (22) can be derived as follows:

$$\eta_m(\mathcal{P}_{\max}) = \frac{\eta_{c,m}(\mathcal{P}_{\max})}{2} \frac{x_m y_m}{y_m + 2d_m}, \quad m = L, P, LP. \quad (26)$$

In Appendix D, we present the details of derivation for Eq. (26). In Eq. (26), $\eta_{c,m}(\mathcal{P}_{\max})$ is the value of the Carnot-engine efficiency which is derived by setting $X_L^V = X_L^{V*}$ in Eqs. (C1) and (C2), and x_m is the asymmetry parameter that is expressed as

$$x_m = \frac{r_m}{y_m}, \quad (27)$$

where

$$r_m = (2\delta\mathcal{Z}_m^A + \mathcal{Z}_m^B + \delta^2\mathcal{Z}_m^C)T, \quad (28)$$

and y_m is the generalized figure of merit, which is described as follows:

$$y_m = (\delta(\mathcal{Z}_m^{A'} + \mathcal{Z}_m^{A''}) + \mathcal{Z}_m^{B'} + \delta^2\mathcal{Z}_m^{C'})T, \quad (29)$$

where $\delta = 1/\xi$. The terms $\mathcal{Z}_m^{\theta}T$ with the superscripts $\theta = A, A', A'', B, B', C$, and C' are given in Eq. (D4). The

parameter d_m in Eq. (26) is given as follows:

$$\begin{aligned} d_L &= \delta \frac{K_{PL} + K_{LP}}{K_{LL}} + \frac{K_{PP}}{K_{LL}} + \delta^2 \quad \text{if } J_L^O > 0, \\ d_P &= \delta \frac{K_{PL} + K_{LP}}{K_{PP}} + \delta^2 \frac{K_{LL}}{K_{PP}} + 1 \quad \text{if } J_P^O > 0, \\ d_{LP} &= \frac{\delta K_{PL} + K_{PP}}{K_{LP}} + \delta^2 \frac{K_{LL}}{K_{LP}} + \delta \quad \text{if } J_L^O, J_P^O > 0. \end{aligned} \quad (30)$$

The parameter d_m is related to the model's thermal conductance and the temperature bias ratio. Utilizing a toy model, as illustrated in Appendix E, we show the possible range of values for d_m . Furthermore, d_m represents the main difference between the voltage probe and the Büttiker probe since our setup includes more complexity and potential for fine tuning to improve efficiency.

For the time-symmetric case $x_m = 1$, Eq. (29) reduces to

$$\mathbb{Z}_m T = (2\delta \mathcal{Z}_m^{A_1} + \mathcal{Z}_m^{B_1} + \delta^2 \mathcal{Z}_m^{C_1}) T, \quad (31)$$

where $A_1 = S_{LL} S_{LP} G_{LL}$, $B_1 = S_{LP}^2 G_{LL}$, and $C_1 = S_{LL}^2 G_{LL}$. We noticed that Eq. (31) is the more compact version of the general figure of merit, which is derived by Mazza *et al.* [42] for a three-terminal genuine heat engine within time-reversal symmetry case.

As discussed below, the formalism developed for the voltage-probe setup can achieve the Büttiker-probe model by imposing the limit of $J_P^O = 0$. When $J_P^O = 0$, Eq. (28) reduces to

$$r_L = \delta^2 \mathcal{Z}_L^C T, \quad (32)$$

where

$$\mathcal{Z}_L^C T = \frac{S_{LL}(\mathbf{B})^2 G_{LL}(\mathbf{B}) T}{K_{LL}}, \quad (33)$$

and correspondingly Eq. (29) reduces to

$$y_L = \delta^2 \mathcal{Z}_L^C T, \quad (34)$$

where

$$\mathcal{Z}_L^C T = y = \frac{G_{LL} S_{LL}(\mathbf{B}) S_{LL}(-\mathbf{B}) T}{K_{LL}} \quad (35)$$

is the general figure of merit of the Büttiker-probe heat engine with broken time-reversal symmetry [34,35,45].

By means of Eqs. (32) and (34), Eq. (27) can be rewritten for the Büttiker-probe engine as follows:

$$x = \frac{S_{LL}(\mathbf{B})}{S_{LL}(-\mathbf{B})}. \quad (36)$$

Finally, in the case that $J_P^O = 0$, Eq. (30) reduces to

$$d_L = \delta^2. \quad (37)$$

Inserting Eqs. (34), (36), and (37) into Eq. (26), the efficiency at maximum output power can be expressed for the Büttiker-probe heat engine as follows:

$$\eta(\mathcal{P}_{\max}) = \frac{\eta_c}{2} \frac{xy}{y+2}, \quad (38)$$

where $\eta_c = \frac{\Delta T_L}{T}$ is the Carnot efficiency of a Büttiker-probe engine. For $x = 1$, the conventional figure of merit for the

Büttiker probe setup can be expressed as

$$\mathbb{Z} T = \frac{G_{LL} S_{LL}^2 T}{K_{LL}} \quad (39)$$

and the maximum output power efficiency for the time-symmetric case is given by $\eta(\mathcal{P}_{\max}) = \frac{\eta_c}{2} \frac{\mathbb{Z} T}{\mathbb{Z} T + 2}$.

F. Efficiency at a given output power

To examine the thermoelectric properties of a three-terminal heat engine at a given output power, the relative gains in power $\Delta \mathcal{P}$ can be expressed as follows:

$$\Delta \mathcal{P} = \frac{\mathcal{P} - \mathcal{P}_{\max}}{\mathcal{P}_{\max}}. \quad (40)$$

The power gain $\Delta \mathcal{P}$ provides us with precise results on the thermoelectric performance of heat engines at a given output power. After simplicity

$$\frac{\mathcal{P}}{\mathcal{P}_{\max}} = 1 + \Delta \mathcal{P} = \frac{J_L^N X_L^V}{J_L^{N*} X_L^{V*}} = \varepsilon(2 - \varepsilon), \quad (41)$$

where $\varepsilon = X_L^V / X_L^{V*}$. The normalized efficiency can be expressed as follows:

$$\frac{\eta_m}{\eta_m(\mathcal{P}_{\max})} = \varepsilon(2 - \varepsilon) \frac{y_m + 2d_m}{2(y_m + d_m) - y_m \varepsilon}. \quad (42)$$

Using Eqs. (34) and (37), one can derive the normalized efficiency for a Büttiker-probe engine [45] as follows:

$$\frac{\eta}{\eta(\mathcal{P}_{\max})} = \varepsilon(2 - \varepsilon) \frac{y + 2}{2(y + 1) - y\varepsilon}. \quad (43)$$

Using Eq. (41), efficiency dependence on the output power is defined as

$$\varepsilon_{\pm} = 1 \pm \sqrt{-\Delta \mathcal{P}}. \quad (44)$$

The plus sign, here, is related to the favorable case where the normalized efficiency goes beyond the $\mathcal{P}/\mathcal{P}_{\max}$ as the external force is increased, and the minus sign describes the opposite case. Furthermore, the ratio $\eta_m/\eta_m(\mathcal{P}_{\max})$ can be expressed as

$$\frac{\eta_m}{\eta_m(\mathcal{P}_{\max})} = (1 + \Delta \mathcal{P}) \frac{y_m + 2d_m}{2(y_m + d_m) - y_m(1 \pm \sqrt{-\Delta \mathcal{P}})}, \quad (45)$$

and for the Büttiker-probe engine [45], Eq. (45) can be rewritten as

$$\frac{\eta}{\eta(\mathcal{P}_{\max})} = (1 + \Delta \mathcal{P}) \frac{y + 2}{2(y + 1) - y(1 \pm \sqrt{-\Delta \mathcal{P}})}. \quad (46)$$

Moreover, the efficiency η_m at a given output power as a function of the power gain $\Delta \mathcal{P}$ can be derived as

$$\eta_m = \frac{\eta_{c,m}}{2} \frac{x_m y_m (1 + \Delta \mathcal{P})}{2(y_m + d_m) - (1 \pm \sqrt{-\Delta \mathcal{P}}) y_m}, \quad (47)$$

and for the Büttiker-probe engine [45], Eq. (47) can be expressed as

$$\eta = \frac{\eta_c}{2} \frac{xy(1 + \Delta \mathcal{P})}{2(y + 1) - (1 \pm \sqrt{-\Delta \mathcal{P}}) y}. \quad (48)$$

III. RESULTS AND DISCUSSION

In this section, we provide numerical results of the theory developed in the previous section. In the linear response regime and within the context of broken time-reversal symmetry, we demonstrate how voltage-probe heat engines can produce higher thermoelectric performance than Büttiker-probe heat engines [34,35,45]. Following that, we uncover similarities and differences in efficiency optimization between the two setups for a given output power.

From Eq. (48), it can be seen that the efficiency of a Büttiker-probe heat engine relies on the parameters x and y . However, the efficiency of a voltage-probe heat engine, in addition to x_m and y_m , depends on the characteristic parameter d_m [see Eq. (47)]. Similar to the work by Brandner *et al.* [34], let us first introduce the following inequality for a voltage-probe heat engine with broken time-reversal symmetry using Eqs. (7), (27), and (29) as follows:

$$\begin{aligned} H_m &\ll y_m \ll 0 \quad \text{for } x_m < 0, \\ H_m &\gg y_m \gg 0 \quad \text{for } x_m > 0, \end{aligned} \quad (49)$$

where

$$H_m = \frac{d_m x_m}{(x_m - 1)^2}. \quad (50)$$

Substituting Eqs. (34) and (37) into the inequality of Eq. (49), the inequality of Büttiker-probe heat engine within broken time-reversal symmetry achieves as follows:

$$\begin{aligned} H &\ll y \ll 0 \quad \text{for } x < 0, \\ H &\gg y \gg 0 \quad \text{for } x > 0, \end{aligned} \quad (51)$$

where y and x are given in Eqs. (35) and (36), respectively, and the function H is given as

$$H = \frac{x}{(x - 1)^2}. \quad (52)$$

Figure 2 illustrates H_m versus x_m for different d_m values. In Appendix E, we display the contour plots of d_m for a triple quantum dot attached to three electronic reservoirs. The results reveal that d_L and d_P are positive, while d_{LP} is negative. Therefore, the positive values of d_m are associated with $m = L, P$, while the negative ones correspond to $m = LP$. In contrast with a Büttiker-probe heat engine, where the function H relies only on x , for a voltage-probe setup, H_m also depends upon d_m , which based on d_m sign and value, bounds on y_m can change. The asymmetric parameter x_m measures the degree of asymmetry due to the presence of an external magnetic field. From Fig. 2, it can be seen that for positive d_m , y_m is located in $[-0.25, 0]$ and $[0, \infty]$ for $x_m < 0$ and $x_m > 0$, respectively. However, for negative d_m , y_m shows a reversed behavior, so that it is located in $[0, 0.25]$ and $[-\infty, 0]$ for $x_m < 0$ and $x_m > 0$, respectively. We noticed that when $x_m = 1$, $\mathbb{Z}_{L(P)} \rightarrow +\infty$ and $\mathbb{Z}_{LP} \rightarrow -\infty$ [see Eq. (31)], corresponding to the work of Mazza *et al.* [42]. When $d_m = 1$, the function H_m coincides with H , as shown by dashed black lines, and in the case that $x = 1$, $\mathbb{Z}T \rightarrow +\infty$ [see Eq. (39)].

Equation (41) shows that the ratio $\mathcal{P}/\mathcal{P}_{\max}$ is a parabolic curve that depends only on the external load ε . The normalized efficiency of a Büttiker-probe heat engine $\eta/\eta(\mathcal{P}_{\max})$,

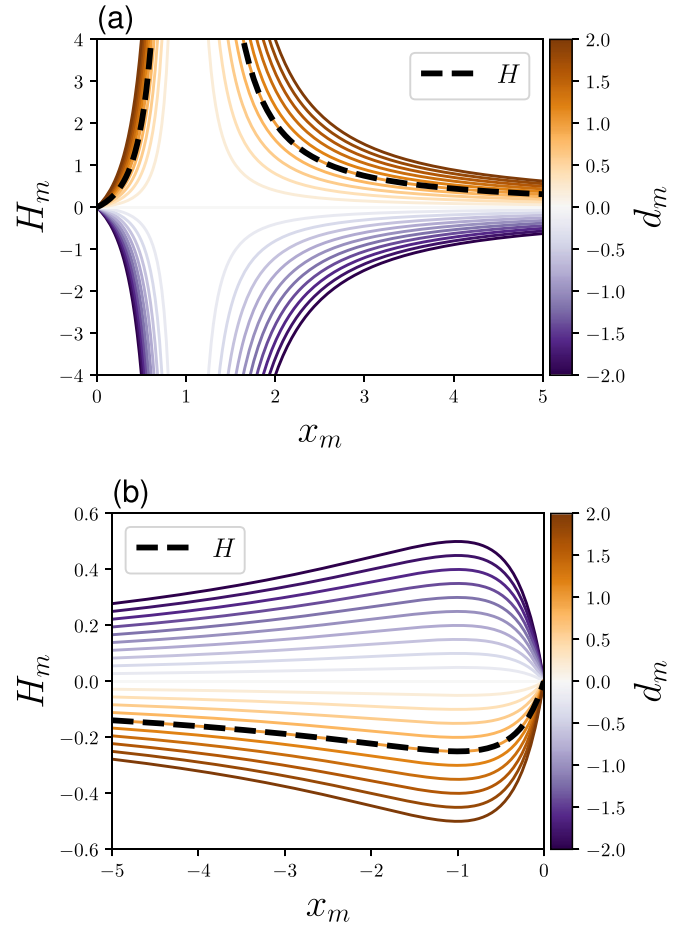


FIG. 2. The function H_m versus x_m for different d_m values are color coded. Dashed black lines display H [Eq. (52)].

expressed in Eq. (43), relies on ε and y . However, the normalized efficiency of a voltage-probe engine $\eta_m/\eta_m(\mathcal{P}_{\max})$, aside from ε and y_m , depends on the additional parameter d_m [see Eq. (42)]. To determine the efficiency dependence on d_m , in Fig. 3, we plot the normalized efficiency of the heat engines as a function of ε when $x_m > 0$. We also plot $\mathcal{P}/\mathcal{P}_{\max}$, shown by dashed black lines. Figure 3(a) displays $\eta/\eta(\mathcal{P}_{\max})$ versus ε for $y > 0$, and Figs. 3(b)–3(f) show the behaviors of $\eta_m/\eta_m(\mathcal{P}_{\max})$ for different d_m values, as a function of ε with y_m which is constrained by $x_m > 0$. Note that as depicted in Figs. 2(a) and 2(b), when $x_m > 0$, $y_{L(P)}$ is located in $[0, \infty]$ for different $d_{L(P)}$, while y_{LP} is located in $[-\infty, 0]$ for different d_{LP} . Therefore, in the region of $x_m > 0$, we set the same signs for d_m and y_m . For the Büttiker-probe heat engine, y is located in $[0, \infty]$ [see dashed black line in Fig. 2(a)].

As illustrated in Fig. 3, for lower external loads $\varepsilon < 1$, Büttiker- and voltage-probe engines show similar characteristics so that the efficiency increases as the output power enhances while it demonstrates a decreasing feature as y and y_m increase. In contrast, for higher external loads $\varepsilon > 1$, the efficiency exhibits different behavior; the optimum efficiency value is achieved for $\varepsilon > 1$, and it is gone up with increasing the absolute value of figures of merit.

Let us now elaborate on how a voltage-probe heat engine with broken time-reversal symmetry can enhance

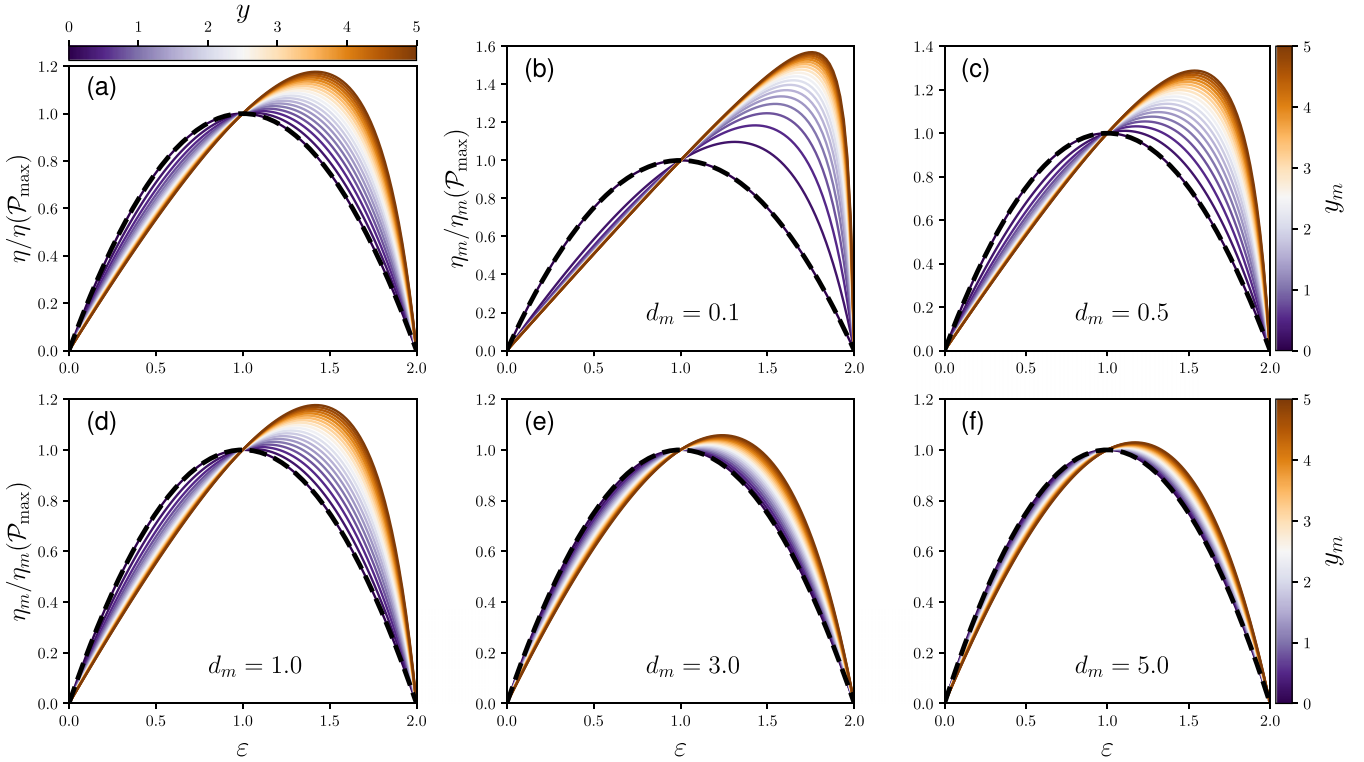


FIG. 3. Ratio $\eta_m/\eta_m(\mathcal{P}_{\max})$ as a function of ε for different values of y_m and d_m in the region of $x_m > 0$. Dashed black lines show $\mathcal{P}/\mathcal{P}_{\max}$. (a) Demonstrates the normalized efficiency of a Büttiker-probe heat engine as a function of ε for different values of y . (b), (c), (d), (e), (f) Show the normalized efficiency of a voltage-probe heat engine for $d_m = 0.1, 0.5, 1.0, 3.0, 5.0$, respectively, and different values of y_m are color coded.

thermoelectric properties at a given output power with respect to a Büttiker-probe setup. From Figs. 3(b) and 3(c), it can be seen that when $d_m < 1.0$, for identical values of y and y_m , the optimum values of efficiency within $\varepsilon > 1$ are larger than those of the Büttiker-probe heat engine [see Fig. 3(a)], implying that for the voltage-probe heat engine, larger efficiency can be achievable at lower y_m compared to y for a Büttiker-probe heat engine. This is due to the presence of the parameter d_m in a voltage-probe setup, contributing to the heat dissipation rate [12] $\dot{Q} = T\dot{S}$. For the voltage-probe setup when $d_m < 1.0$, \dot{Q} decreases more compared to that of the Büttiker-probe heat engine, giving rise to the larger optimum values of efficiency for the voltage-probe heat engine in the region of $\varepsilon > 1$. However, the opposite occurs when $d_m > 1.0$, so the optimum values of efficiency diminish compared with that of the Büttiker-probe engine, as shown in Figs. 3(e) and 3(f). Furthermore, in the case that $d_m = 1.0$, the normalized efficiency of the voltage-probe setup exactly shows the same behavior as that of a Büttiker-probe heat engine [compare Figs. 3(a) and 3(d)]. Therefore, it is interesting that for a voltage-probe heat engine, the parameter d_m is significantly contributing to changing the normalized-efficiency values at a given output power.

Equation (44) indicates that ε as a function of power gain ($\Delta\mathcal{P}$) has two branches. To examine the efficiency dependence on $\Delta\mathcal{P}$, in Fig. 4, we plot the normalized efficiency as a function of $\Delta\mathcal{P}$ for the favorable case ε_+ . Figure 4(a) exhibits the normalized efficiency of the Büttiker-probe heat engine as a function of $\Delta\mathcal{P}$ [see Eq. (46)]. We display the normalized

efficiency of the voltage-probe engines as a function of $\Delta\mathcal{P}$ for different d_m as shown in Figs. 4(b)–4(f).

From the color-coded lines in Fig. 4, one can observe that increasing y_m (y) for a fixed $\Delta\mathcal{P}$ results in enhanced efficiency of a voltage-probe (Büttiker-probe) heat engine. Figure 4(a) indicates that for a Büttiker-probe heat engine, most normalized-efficiency curves monotonically rise as the output power increases (from -1 to 0). However, for the voltage-probe engines, when $d_m < 1.0$, the normalized efficiency curves mostly nonmonotonically change as power gains change, as shown in Figs. 4(b) and 4(c). Thus, in the case that $d_m < 1.0$, the voltage-probe heat engine achieves a larger efficiency value at lower values of y_m compared to a Büttiker probe. When $d_m > 1.0$, the normalized efficiency curves monotonically increase as $\Delta\mathcal{P}$ changes, as depicted in Figs. 4(e) and 4(f). Therefore, the voltage-probe engine cannot enhance the optimum value of efficiency, even if y_m increases. For some values of y_m in Fig. 4, it can be noticed that a larger efficiency can be achieved when the output power \mathcal{P} is less than the maximum output power \mathcal{P}_{\max} . This implies that there is a fundamental tradeoff between the efficiency and output power in thermoelectric performance optimization of both Büttiker- and voltage-probe engines. However, the unique feature of our study is not merely the identification of this tradeoff, but the recognition of how the parameter d_m can be utilized to manipulate it in voltage-probe heat engines, compared to Büttiker-probe setup, particularly in the context of broken time-reversal symmetry. In other words, this tradeoff is tunable by adjusting dm , allowing us to optimize the

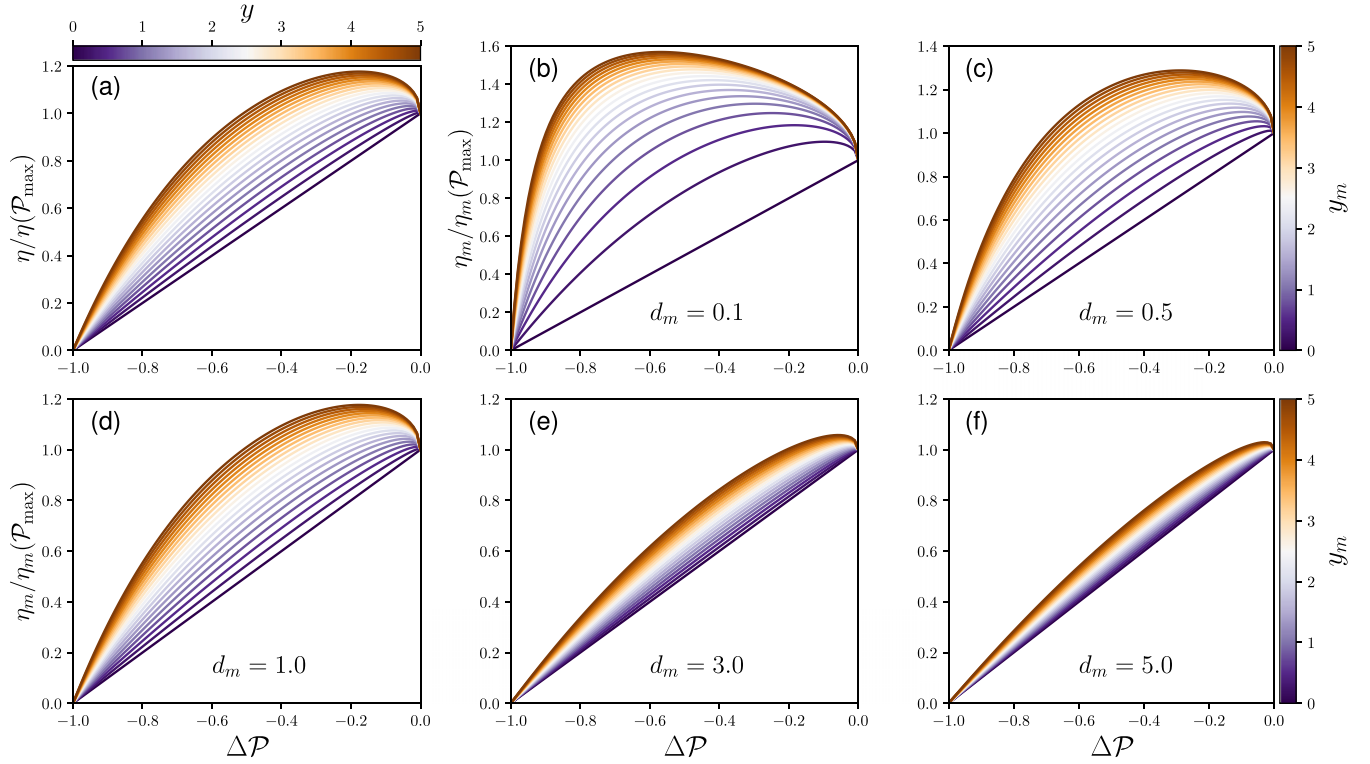


FIG. 4. The normalized efficiency as a function of power gains $\Delta\mathcal{P}$ for the favorable case ε_+ . The rest parameters are set the same as the Fig. 3.

thermoelectric performance in a way previously considered unattainable. In contrast with a Büttiker-probe heat engine, whose efficiency depends on y and $\Delta\mathcal{P}$, the normalized efficiency of the voltage-probe engine indicates that, in practice, the operational conditions of the voltage-probe engines are optimized based on d_m , $\Delta\mathcal{P}$, and y_m .

Furthermore, the asymmetry parameter x_m is also vital to optimize the performance of a heat engine with broken time-reversal symmetry at a given output power. In the case that $y_m = H_m$, for different cases expressed in Eqs. (21) and (22), we can derive the bounds on efficiency η_m by means of Eq. (47) as follows:

$$\eta_m^{\text{bound}} = \frac{\eta_{c,m}}{2} \frac{x_m^2(1 + \Delta\mathcal{P})}{2(x_m^2 - x_m + 1) - (1 \pm \sqrt{-\Delta\mathcal{P}})x_m}. \quad (53)$$

We noticed that when $J_P^O = 0$, Eq. (53) becomes equal to the general bound on efficiency obtained by Zhang *et al.* [45] for the Büttiker-probe heat engine; thus, the general bounds on efficiency are identical for these two setups. The difference is that for the voltage-probe heat engine, there are three possibilities for the bound efficiency of the heat engine based on Eqs. (21) and (22). To optimize the general bound on the heat-engine efficiency, we solve the relation $\partial\eta_m^{\text{bound}}/\partial x_m = 0$. We found $x_m = 0$ and $x_m = \pm 1$ are three possible extreme points. To analyze the dependence of the bound efficiency (η_m^{bound}) on the x_m as well as $\Delta\mathcal{P}$, in Fig. 5, we display η_m^{bound} as a function of x_m for different $\Delta\mathcal{P}$ and for both favorable and unfavorable case ε_{\pm} , as illustrated in Figs. 5(a) and 5(b), respectively. It can be seen that the new universal bounds on efficiency are obtained for different $\Delta\mathcal{P}$, and that the maximum-efficiency

value is achieved somewhere around the symmetric point $x_m = 1$. From Fig. 5(a) it can be observed that the bound efficiency reaches η_c only for $x_m = 1$ and decreases rapidly as the asymmetry parameter deviates from 1. For $x_m \neq 1$ the Carnot efficiency can never be obtained due to the limitations imposed on the Onsager coefficients [see Eq. (7)]. In the limit $x_m \rightarrow \pm\infty$ functions asymptotically approach the value $\frac{\eta_{c,m}}{4}(1 + \Delta\mathcal{P})$, indicating that the bound on efficiency depends only on the power gain in these regions. Moreover, it is highlighted that the associated bound efficiency increases as $\Delta\mathcal{P}$ changes from -1 to 0 , implying that it is in principle possible to enhance the thermoelectric performance of quantum heat engines at a given output power by breaking time-reversal symmetry. When $\Delta\mathcal{P} = 0$, maximum output power efficiency can be achieved [see dashed black curves in Figs. 5(a) and 5(b)], which corresponds with the results of Brandner *et al.* [32,34]. Clearly, the well-known Curzon-Ahlborn limit ($\eta_{c,m}/2$) is recovered not only for the symmetric point $x_m = 1$, shown by red spot in Fig. 5(a), but also for other cases. This implies that the CA limit is readily accessible in the context of broken time-reversal symmetry and in the linear response regime. Additionally, the CA limit can be surpassed when time-reversal symmetry is broken, as shown in Fig. 5(a). However, it is not overcome in the unfavorable case, as indicated in Fig. 5(b). For comparison, we include the bound on maximum output power efficiency with broken time-reversal symmetry obtained by Benenti *et al.* [21] (black solid line). This is achieved only from the constraint of the second law of thermodynamics, leading to the possibility of dissipationless transport. In this case the quantum heat engine can operate at Carnot efficiency with finite output power [12].

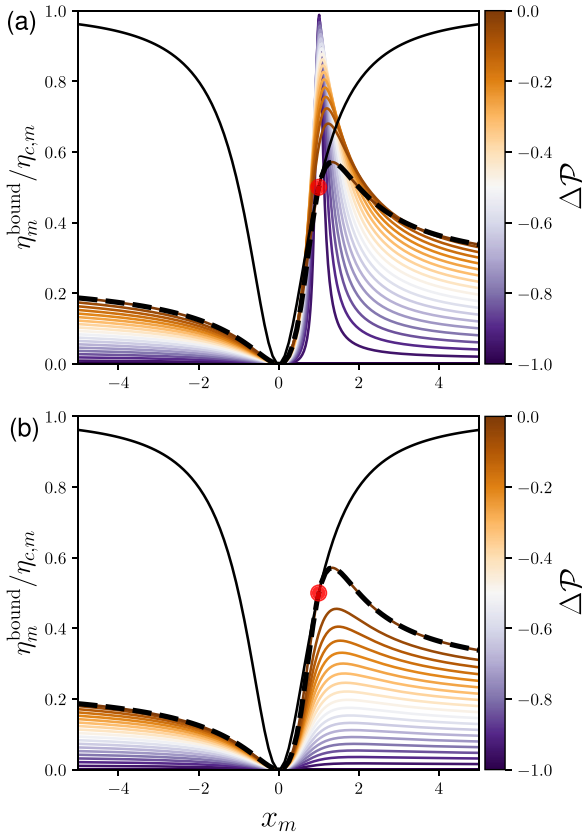


FIG. 5. Efficiency bound $\eta_m^{\text{bound}}/\eta_{c,m}$ versus the asymmetry parameter x_m and the power gain $\Delta\mathcal{P}$ for (a): favorable case ε_+ and (b): unfavorable case ε_- . The intersecting points of the red-circle lines represent the Curzon-Ahlborn limit (CA) efficiency in the linear response regime $\eta_{CA,m} = \eta_{c,m}/2$. For comparison, the bounds obtained by Benenti *et al.* [21] only from thermodynamic entropy production $\dot{S} > 0$ (black solid line) and Brandner *et al.* [34] on three-terminal setup with considering the role of current conservation (black dashed lines) are included.

IV. CONCLUSION

Within broken time-reversal symmetry and in the linear response regime, the optimal performance at a given output power of a voltage-probe heat engine is examined. The normalized efficiency at a given output power $\eta_m/\eta_m(\mathcal{P}_{\text{max}})$, the asymmetric parameter x_m , the general figure of merit y_m , and the parameter d_m are first introduced in our work. $\eta_m/\eta_m(\mathcal{P}_{\text{max}})$, y_m , and d_m are classified into three cases with subscripts $m = L, P$, and LP , based on the heat current(s) extracted from the reservoir L , reservoir P , and both reservoirs L and P , respectively. This work aims to find out how a voltage-probe heat engine, where the probe reservoir is adjusted to block charge flows and only allow heat flows can enhance the efficiency at a given output power of the quantum heat engine compared to a Büttiker-probe setup, where the probe reservoir blocks both heat and charge flows. We also analytically prove that by applying the condition of zero heat flows throughout the probe reservoir and the scattering region all thermoelectric properties of a Büttiker-probe heat engine can be achieved. Our results reveal that, unlike a Büttiker-probe heat engine, a voltage-probe device due to the parameter d_m ,

can change the upper and lower bounds on y_m . In contrast with a Büttiker-probe heat engine, where the general figure of merit y and power gain $\Delta\mathcal{P}$ influence the normalized efficiency at a given output power, the voltage-probe heat engine, via the parameter d_m , offers an additional capability: it modifies both the upper and lower bounds of y_m . This behavior is not evident in a Büttiker-probe heat engine. Specifically, the efficiency at a given output power is controlled by the parameter d_m , and optimum efficiency increases when $d_m < 1$. It is also found that, like a Büttiker-probe heat engine, the universal bounds on the efficiency of quantum heat engines with broken time-reversal symmetry are obtained, and the efficiency at a given output power can overcome the Curzon-Ahlborn limit. Tuning of parameters x_m , d_m , and y_m in real experimental setups is indeed feasible. Through the careful choice of materials, external conditions, and system configurations (as demonstrated in our toy model), these parameters can be effectively controlled, paving the way for optimizing the tradeoff between output power and efficiency in thermoelectric systems. One can also extend our theory to a genuine three-terminal heat engine that Mazza *et al.* utilized in their work [42]. This setup is more complex than a voltage-probe heat engine and, as a result, it would be beneficial to enhance the normalized efficiency at a given output power compared to the voltage-probe or Büttiker-probe heat engines.

APPENDIX A: SCATTERING APPROACH WITHIN THE LINEAR RESPONSE REGIME

The coherent flow of heat and particles via a conductor without electron-electron interactions can be defined through the Landauer-Büttiker formalism. Taking the assumption that all phase-breaking and dissipative processes are restricted to the reservoirs, the heat and particle currents can be written in terms of the scattering characteristics of the scattering region [50]. For a multiterminal setup, the particle and heat currents flowing into the scattering region from the k th reservoir can be described using the Landauer-Büttiker formalism as follows:

$$J_\alpha^N = \frac{1}{h} \int dE \sum_{\alpha \neq \beta} \mathcal{T}_{\alpha\beta}(E)(f_\alpha(E) - f_\beta(E)),$$

$$J_\alpha^Q = \frac{1}{h} \int dE (E - \mu_\alpha) \sum_{\alpha \neq \beta} \mathcal{T}_{\alpha\beta}(E)(f_\alpha(E) - f_\beta(E)), \quad (\text{A1})$$

where h is the Planck's constant, $\mathcal{T}_{\alpha\beta}$ is the transmission probability from reservoir α to β , and $f_\alpha(E)$ is the Fermi function of the respective reservoirs described as $f_\alpha(E) = \{\exp[(E - \mu_\alpha)/k_B T] + 1\}^{-1}$.

APPENDIX B: ONSAGER COEFFICIENTS

Using Eq. (A1), the Onsager coefficients of Eq. (3) can be obtained from the linear expansion of the currents J_α^N and J_α^Q ($J = \mathcal{L}X$) as follows:

$$\mathcal{L}_{11} = \frac{T}{h} \int_{-\infty}^{\infty} f'(-E)(\mathcal{T}_{LP} + \mathcal{T}_{LR}) dE,$$

$$\mathcal{L}_{12} = \frac{T}{h} \int_{-\infty}^{\infty} f'(-E)(E - \mu)(\mathcal{T}_{LP} + \mathcal{T}_{LR}) dE,$$

$$\begin{aligned}
\mathcal{L}_{13} &= \frac{T}{h} \int_{-\infty}^{\infty} -f'(-E) \mathcal{T}_{LP} dE, \\
\mathcal{L}_{14} &= \frac{T}{h} \int_{-\infty}^{\infty} f'(-E) (-E - \mu) \mathcal{T}_{LP} dE, \\
\mathcal{L}_{21} &= \mathcal{L}_{12}, \\
\mathcal{L}_{22} &= \frac{T}{h} \int_{-\infty}^{\infty} f'(-E) (E - \mu)^2 (\mathcal{T}_{LP} + \mathcal{T}_{LR}) dE, \\
\mathcal{L}_{23} &= \mathcal{L}_{14}, \\
\mathcal{L}_{24} &= \frac{T}{h} \int_{-\infty}^{\infty} f'(-E) (-E - \mu)^2 \mathcal{T}_{LP} dE, \\
\mathcal{L}_{31} &= \frac{T}{h} \int_{-\infty}^{\infty} -f'(-E) \mathcal{T}_{PL} dE, \\
\mathcal{L}_{32} &= \frac{T}{h} \int_{-\infty}^{\infty} f'(-E) (-E - \mu) \mathcal{T}_{PL} dE, \\
\mathcal{L}_{33} &= \frac{T}{h} \int_{-\infty}^{\infty} f'(-E) (\mathcal{T}_{PL} + \mathcal{T}_{PR}) dE, \\
\mathcal{L}_{34} &= \frac{T}{h} \int_{-\infty}^{\infty} f'(-E) (E - \mu) (\mathcal{T}_{PL} + \mathcal{T}_{PR}) dE, \\
\mathcal{L}_{41} &= \mathcal{L}_{32}, \\
\mathcal{L}_{42} &= \frac{T}{h} \int_{-\infty}^{\infty} f'(-E) (-E - \mu)^2 \mathcal{T}_{PL} dE, \\
\mathcal{L}_{43} &= \mathcal{L}_{34}, \\
\mathcal{L}_{44} &= \frac{T}{h} \int_{-\infty}^{\infty} f'(-E) (E - \mu)^2 (\mathcal{T}_{PL} + \mathcal{T}_{PR}) dE, \quad (\text{B1})
\end{aligned}$$

where $f'(E)$ is the derivative of the Fermi-Dirac distribution with respect to the energy. As mentioned before, in a voltage-probe heat engine, the probe reservoir blocks particle flows ($J_P^N = 0$); thus, X_P^V in Eq. (3) can be derived as follows:

$$X_P^V = \frac{-(\mathcal{L}_{31} X_L^V + \mathcal{L}_{32} X_L^T + \mathcal{L}_{34} X_P^T)}{\mathcal{L}_{33}}. \quad (\text{B2})$$

Setting Eq. (B2) into Eq. (3), and after some algebras, the Onsager coefficients of Eq. (4) can be expressed as follows:

$$\begin{aligned}
\mathcal{L}'_{11} &= \frac{\mathcal{L}_{33} \mathcal{L}_{11} - \mathcal{L}_{13} \mathcal{L}_{31}}{\mathcal{L}_{33}}, \quad \mathcal{L}'_{12} = \frac{\mathcal{L}_{33} \mathcal{L}_{12} - \mathcal{L}_{13} \mathcal{L}_{32}}{\mathcal{L}_{33}}, \\
\mathcal{L}'_{13} &= \frac{\mathcal{L}_{14} \mathcal{L}_{33} - \mathcal{L}_{13} \mathcal{L}_{34}}{\mathcal{L}_{33}}, \quad \mathcal{L}'_{21} = \frac{\mathcal{L}_{21} \mathcal{L}_{33} - \mathcal{L}_{23} \mathcal{L}_{31}}{\mathcal{L}_{33}},
\end{aligned}$$

$$\begin{aligned}
\mathcal{L}'_{22} &= \frac{\mathcal{L}_{33} \mathcal{L}_{22} - \mathcal{L}_{23} \mathcal{L}_{32}}{\mathcal{L}_{33}}, \quad \mathcal{L}'_{23} = \frac{\mathcal{L}_{24} \mathcal{L}_{33} - \mathcal{L}_{23} \mathcal{L}_{34}}{\mathcal{L}_{33}}, \\
\mathcal{L}'_{31} &= \frac{\mathcal{L}_{41} \mathcal{L}_{33} - \mathcal{L}_{43} \mathcal{L}_{31}}{\mathcal{L}_{33}}, \quad \mathcal{L}'_{32} = \frac{\mathcal{L}_{42} \mathcal{L}_{33} - \mathcal{L}_{43} \mathcal{L}_{32}}{\mathcal{L}_{33}}, \\
\mathcal{L}'_{33} &= \frac{\mathcal{L}_{44} \mathcal{L}_{33} - \mathcal{L}_{43} \mathcal{L}_{34}}{\mathcal{L}_{33}}, \quad (\text{B3})
\end{aligned}$$

where \mathcal{L}_{ab} are given in Eq. (B1). Analogously, placing $J_P^Q = 0$ into Eq. (4), the Onsager coefficients of Eq. (5) are expressed as follows:

$$\begin{aligned}
\mathcal{L}''_{11} &= \frac{\mathcal{L}'_{11} \mathcal{L}'_{33} - \mathcal{L}'_{13} \mathcal{L}'_{31}}{\mathcal{L}'_{33}}, \quad \mathcal{L}''_{12} = \frac{\mathcal{L}'_{12} \mathcal{L}'_{33} - \mathcal{L}'_{13} \mathcal{L}'_{32}}{\mathcal{L}'_{33}}, \\
\mathcal{L}''_{21} &= \frac{\mathcal{L}'_{21} \mathcal{L}'_{33} - \mathcal{L}'_{23} \mathcal{L}'_{31}}{\mathcal{L}'_{33}}, \quad \mathcal{L}''_{22} = \frac{\mathcal{L}'_{22} \mathcal{L}'_{33} - \mathcal{L}'_{23} \mathcal{L}'_{32}}{\mathcal{L}'_{33}}, \quad (\text{B4})
\end{aligned}$$

where \mathcal{L}'_{ab} are given in Eq. (B3).

APPENDIX C: CARNOT EFFICIENCY

In any steady-state heat-to-work conversion device, the thermoelectric efficiency is bounded from above by the Carnot engine efficiency η_c , which can be calculated by placing the condition of zero-entropy production rate ($\dot{S} = 0$). For a three-terminal device, it can be derived by analogy with the Carnot efficiency of a two-terminal setup and described in terms of three cases defined in Eqs. (21) and (22). If the heat current is only absorbed from either reservoir P ($J_P^Q > 0$) or L ($J_L^Q > 0$), the Carnot efficiency is derived as

$$\eta_{c,L(P)} = \frac{1}{T} \left[\frac{\Delta T_P J_P^Q + \Delta T_L J_L^Q}{J_{L,(P)}^Q} \right], \quad (\text{C1})$$

index L in the denominator is substituted by P if the heat current flows from electrode L into the scattering region. Analogously, if heat current is extracted from both reservoirs P and L ($J_L^Q > 0$ and $J_P^Q > 0$), it gives

$$\eta_{c,LP} = \frac{1}{T} \left[\frac{\Delta T_P J_P^Q + \Delta T_L J_L^Q}{J_L^Q + J_P^Q} \right]. \quad (\text{C2})$$

The Carnot efficiency of the Büttiker-probe heat engine [45] is obtained by imposing the condition of $J_P^Q = 0$. Therefore, for a Büttiker-probe device it is expressed as $\eta_c = \frac{\Delta T_L}{T}$.

APPENDIX D: EFFICIENCY AT MAXIMUM OUTPUT POWER WITH BROKEN TIME-REVERSAL SYMMETRY

Here, we mathematically derive Eq. (26). Setting Eqs. (24) and (25) into the efficiency expressions detailed in Eqs. (21) and (22), it is possible to obtain efficiency at maximum output power for a voltage-probe engine as follows:

$$\eta_L(P_{\max}) = \frac{1}{2T} \frac{[Z_L^B T \delta^{-1} + 2Z_L^A T] \Delta T_P + Z_L^C T \Delta T_L}{\delta^{-1} [Z_L^A T + 2(\frac{K_{LP}}{K_{LL}})] + Z_L^C T + 2}, \quad (\text{D1})$$

$$\eta_P(P_{\max}) = \frac{1}{2T} \frac{[Z_P^C T \delta + 2Z_P^A T] \Delta T_L + Z_P^B T \Delta T_P}{\delta [Z_P^A T + 2(\frac{K_{PL}}{K_{PP}})] + Z_P^B T + 2}, \quad (\text{D2})$$

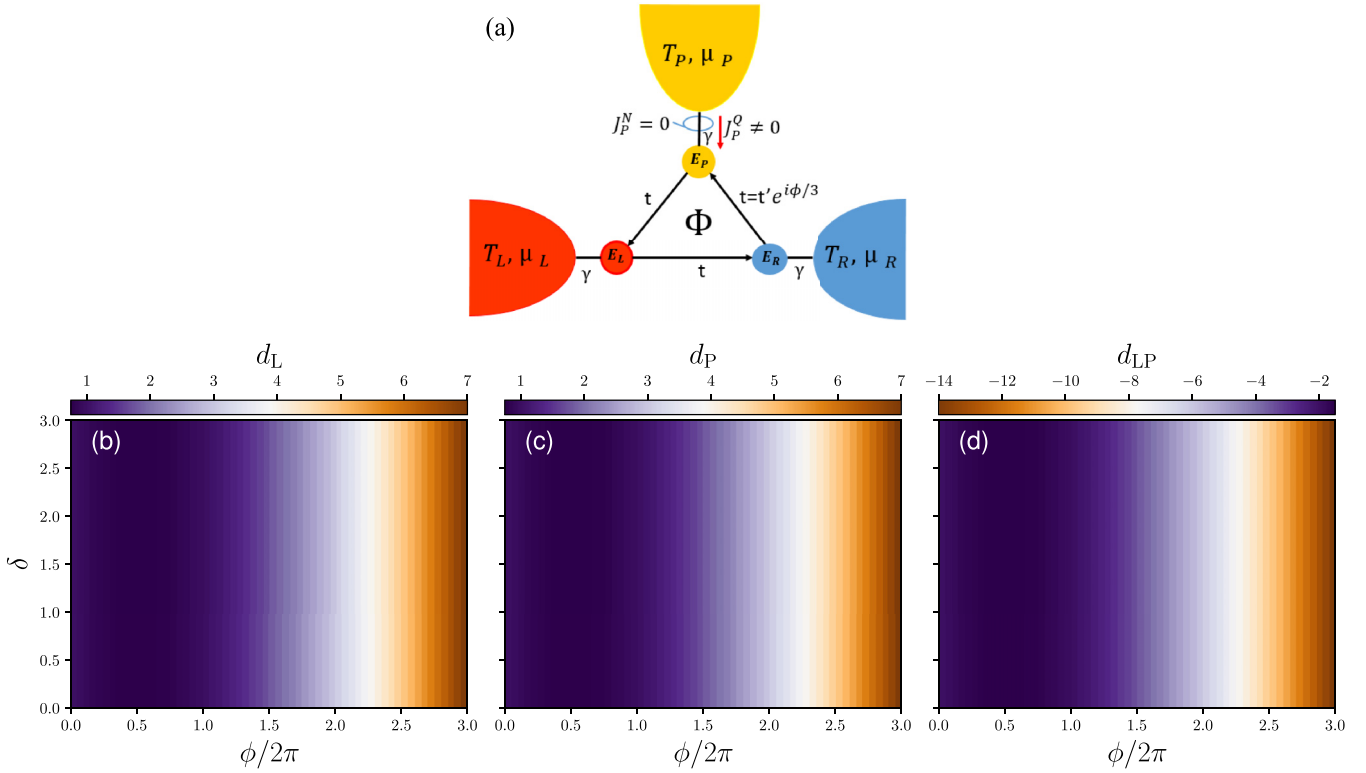


FIG. 6. (a) Shows a voltage-probe system consisting of a triple quantum dot with a single energy level, subjected to the external magnetic field (\mathbf{B}) and connected to three electronic reservoirs, labeled L , P , and R , in different temperatures ($T_L > T_P > T_R$) and chemical potentials μ_L , μ_P , and μ_R . (b)–(d) Exhibit the contour plots of d_L , d_P , and d_{LP} , respectively, as a function of ϕ and δ for the system illustrated in (a). The atomic site energies of the quantum dots connected to the reservoirs L , P , and R are $E_L - \mu = 1.0 k_B T$, $E_P - \mu = 1.0 k_B T$, and $E_R - \mu = 1.0 k_B T$, respectively, where $\mu = \mu_R = 0$, $T = T_R$, and $k_B T = 1$. Coupling parameter: $\gamma_L = \gamma_P = \gamma_R = \gamma = 0.5 k_B T$. Hopping energy parameter between two atomic sites: $t = t' e^{i\phi/3}$, where $\phi = 2\pi \Phi / \Phi_0$ (Φ_0 is quantum flux) and $t' = 1.0 k_B T$.

$$\eta_{LP}(\mathcal{P}_{\max}) = \frac{1}{2T} \frac{[Z_{LP}^B T \delta^{-1} + 2Z_{LP}^A T] \Delta T_P + Z_{LP}^C T \Delta T_L}{\delta^{-1} [Z_{LP}^{B'} T + Z_{LP}^{A''} T + 2(\frac{K_{PP}}{K_{LP}} + 1)] + 2(\frac{K_{PL} + K_{LL}}{K_{LP}}) + Z_{LP}^{A'} T + Z_{LP}^{C'} T}, \quad (D3)$$

where $Z_m^\theta T$ are the generalized figures of merit for a voltage-probe heat engine, given as follows:

$$Z_L^\theta T = \frac{\theta T}{K_{LL}}, \quad Z_P^\theta T = \frac{\theta T}{K_{PP}}, \quad Z_{LP}^\theta T = \frac{\theta T}{K_{LP}}, \quad (D4)$$

where $\theta = A, A', A'', B, B', C, C'$ is defined as follows:

$$\begin{aligned} A &= S_{LL}(\mathbf{B}) S_{LP}(\mathbf{B}) G_{LL}(\mathbf{B}), & A' &= S_{LL}(\mathbf{B}) S_{LP}(-\mathbf{B}) G_{LL}(\mathbf{B}), & A'' &= S_{LP}(\mathbf{B}) S_{LL}(-\mathbf{B}) G_{LL}(\mathbf{B}), \\ B &= S_{LP}(\mathbf{B})^2 G_{LL}(\mathbf{B}), & B' &= S_{LP}(\mathbf{B}) S_{LP}(-\mathbf{B}) G_{LL}(\mathbf{B}), \\ C &= S_{LL}(\mathbf{B})^2 G_{LL}(\mathbf{B}), & C' &= S_{LL}(\mathbf{B}) S_{LL}(-\mathbf{B}) G_{LL}(\mathbf{B}). \end{aligned} \quad (D5)$$

Equation (D3) can also be written in terms of the corresponding Carnot efficiency as follows:

$$\begin{aligned} \eta_L(\mathcal{P}_{\max}) &= \frac{\eta_{c,L}(\mathcal{P}_{\max})}{2} \frac{Z_L^C T \delta^2 + 2\delta Z_L^A T + Z_L^B T}{\delta T (Z_L^{A'} + Z_L^{A''}) + Z_L^{B'} T + \delta^2 T Z_L^{C'} + 2(\frac{\delta K_{PL} + K_{LP}}{K_{LL}}) + 2(\frac{K_{PP}}{K_{LL}}) + 2\delta^2} \\ &= \frac{\eta_{c,L}(\mathcal{P}_{\max})}{2} \frac{r_L}{y_L + 2d_L}, \end{aligned} \quad (D6)$$

$$\begin{aligned} \eta_P(\mathcal{P}_{\max}) &= \frac{\eta_{c,P}(\mathcal{P}_{\max})}{2} \frac{Z_P^C T \delta^2 + 2\delta Z_P^A T + Z_P^B T}{\delta T (Z_P^{A'} + Z_P^{A''}) + Z_P^{B'} T + \delta^2 T Z_P^{C'} + 2\delta(\frac{K_{PL} + K_{LP}}{K_{PP}}) + 2\delta^2(\frac{K_{LL}}{K_{PP}}) + 2} \\ &= \frac{\eta_{c,P}(\mathcal{P}_{\max})}{2} \frac{r_P}{y_P + 2d_P}, \end{aligned} \quad (D7)$$

$$\begin{aligned}\eta_{LP}(\mathcal{P}_{\max}) &= \frac{\eta_{c,LP}(\mathcal{P}_{\max})}{2} \frac{\mathcal{Z}_{LP}^C T \delta^2 + 2\delta \mathcal{Z}_{LP}^A T + \mathcal{Z}_{LP}^B T}{\delta T (\mathcal{Z}_{LP}^{A'} + \mathcal{Z}_{LP}^{A''}) + \mathcal{Z}_{LP}^{B'} T + \delta^2 T \mathcal{Z}_{LP}^{C'} + 2\left(\frac{\delta K_{PL} + K_{PP}}{K_{LP}}\right) + 2\delta^2 \left(\frac{K_{LL}}{K_{LP}}\right) + 2\delta} \\ &= \frac{\eta_{c,LP}(\mathcal{P}_{\max})}{2} \frac{r_{LP}}{y_{LP} + 2d_{LP}}.\end{aligned}\quad (\text{D8})$$

After some algebras, maximum output power efficiency for a voltage-probe heat engine can be obtained as follows:

$$\eta_m(\mathcal{P}_{\max}) = \frac{\eta_{c,m}(\mathcal{P}_{\max})}{2} \frac{x_m y_m}{y_m + 2d_m}, \quad m = L, P, LP \quad (\text{D9})$$

where $x_m = \frac{r_m}{y_m}$.

APPENDIX E: TOY MODEL

In this Appendix, the primary purpose of introducing the toy model in the presence of an external magnetic field is to investigate numerically the sign and the range of the parameter d_m [see Eq. (30)] under various conditions, and we have not explicitly examined the Aharonov-Bohm effect within this framework. For simplicity, we employed the wide-band limit (WBL) approximation, where the couplings of reservoirs to the scatterings region remain independent of energy.

Figure 6(a) depicts a voltage-probe engine consisting of a triple quantum dot with a single energy level, subjected to an external magnetic field \mathbf{B} which are connected to three electronic reservoirs, labeled L , P , and R , in different temperatures ($T_L > T_P > T_R$) and chemical potentials μ_L , μ_P , and μ_R .

For simplicity, the coupling strengths to reservoirs L , P , and R are taken equal to γ , and E_α ($\alpha = L, P, R$) denotes the atomic site energy of respective quantum dots. To describe the electronic structure as well as the transport properties of the setup under consideration, we utilize the nonequilibrium Green function technique [50]. Once the transmission function is obtained, through the Onsager matrix [expressed in Eq. (4)], one can find all driven currents in the setup. Figures 6(b)–6(d) demonstrate the plots of d_L , d_P , and d_{LP} as a function of ϕ and δ . It can be seen that d_L and d_P are positive as a function of δ and ϕ , while d_{LP} is negative. It is evident that by tuning the ratio $\delta = X_L^T / X_L^P$ and ϕ , we can tune the value of the parameter d_m in our setup.

-
- [1] Y. Dubi and M. Di Ventra, *Rev. Mod. Phys.* **83**, 131 (2011).
 - [2] B. Sothmann, R. Sánchez, and A. N. Jordan, *Nanotechnology* **26**, 032001 (2015).
 - [3] R. S. Whitney, *Phys. Rev. B* **91**, 115425 (2015).
 - [4] T. E. Humphrey, R. Newbury, R. P. Taylor, and H. Linke, *Phys. Rev. Lett.* **89**, 116801 (2002).
 - [5] J. Eglinton and K. Brandner, *Phys. Rev. E* **105**, L052102 (2022).
 - [6] K. Hammam, Y. Hassouni, R. Fazio, and G. Manzano, *New J. Phys.* **23**, 043024 (2021).
 - [7] P. A. Erdman, F. Mazza, R. Bosisio, G. Benenti, R. Fazio, and F. Taddei, *Phys. Rev. B* **95**, 245432 (2017).
 - [8] G. Haack and F. Giazotto, *Phys. Rev. B* **100**, 235442 (2019).
 - [9] A. Ahmadi Fouladi and J. Vahedi, *J. Res. Many-body Syst.* **12**, 1 (2023).
 - [10] F. L. Curzon and B. Ahlborn, *Am. J. Phys.* **43**, 22 (1975).
 - [11] A. De Vos, *J. Phys. Chem.* **95**, 4534 (1991).
 - [12] G. Benenti, G. Casati, K. Saito, and R. Whitney, *Phys. Rep.* **694**, 1 (2017).
 - [13] B. Jiménez de Cisneros and A. C. Hernández, *Phys. Rev. Lett.* **98**, 130602 (2007).
 - [14] B. Andresen, *Angew. Chem., Int. Ed.* **50**, 2690 (2011).
 - [15] M. Esposito, R. Kawai, K. Lindenberg, and C. Van den Broeck, *Phys. Rev. Lett.* **105**, 150603 (2010).
 - [16] R. S. Whitney, *Phys. Rev. Lett.* **112**, 130601 (2014).
 - [17] A. Ryabov and V. Holubec, *Phys. Rev. E* **93**, 050101(R) (2016).
 - [18] V. Holubec and A. Ryabov, *J. Stat. Mech.: Theory Exp.* (2016) 073204.
 - [19] V. Holubec and A. Ryabov, *Phys. Rev. E* **92**, 052125 (2015).
 - [20] R. Long and W. Liu, *Phys. Rev. E* **94**, 052114 (2016).
 - [21] G. Benenti, K. Saito, and G. Casati, *Phys. Rev. Lett.* **106**, 230602 (2011).
 - [22] O. Entin-Wohlman, Y. Imry, and A. Aharony, *Phys. Rev. B* **82**, 115314 (2010).
 - [23] O. Entin-Wohlman and A. Aharony, *Phys. Rev. B* **85**, 085401 (2012).
 - [24] J.-H. Jiang, O. Entin-Wohlman, and Y. Imry, *Phys. Rev. B* **85**, 075412 (2012).
 - [25] S. Bedkhal, M. Bandyopadhyay, and D. Segal, *Eur. Phys. J. B* **86**, 506 (2013).
 - [26] S. Bedkhal, M. Bandyopadhyay, and D. Segal, *Phys. Rev. B* **88**, 155407 (2013).
 - [27] J. Behera, S. Bedkhal, B. K. Agarwalla, and M. Bandyopadhyay, *arXiv:2303.09202*.
 - [28] K. Saito, G. Benenti, G. Casati, and T. Prosen, *Phys. Rev. B* **84**, 201306(R) (2011).
 - [29] M. Horvat, T. Prosen, G. Benenti, and G. Casati, *Phys. Rev. E* **86**, 052102 (2012).
 - [30] S. A. Amelkin, B. Andresen, J. M. Burzler, K. H. Hoffmann, and A. M. Tsirlin, *J. Phys. D: Appl. Phys.* **37**, 1400 (2004).
 - [31] S. Amelkin, B. Andresen, J. Burzler, K. Hoffmann, and A. Tsirlin, *J. Non-Equilib. Thermodyn.* **30**, 67 (2005).
 - [32] K. Brandner and U. Seifert, *Phys. Rev. E* **91**, 012121 (2015).
 - [33] V. Balachandran, G. Benenti, and G. Casati, *Phys. Rev. B* **87**, 165419 (2013).
 - [34] K. Brandner, K. Saito, and U. Seifert, *Phys. Rev. Lett.* **110**, 070603 (2013).
 - [35] K. Brandner and U. Seifert, *New J. Phys.* **15**, 105003 (2013).
 - [36] M. Xi, R. Wang, J. Lu, and J.-H. Jiang, *Chin. Phys. Lett.* **38**, 088801 (2021).

- [37] U. Eckern and K. I. Wysokiński, *New J. Phys.* **22**, 013045 (2020).
- [38] R. Sánchez and M. Büttiker, *Phys. Rev. B* **83**, 085428 (2011).
- [39] D. Sánchez and L. Serra, *Phys. Rev. B* **84**, 201307(R) (2011).
- [40] B. Sothmann and M. Büttiker, *Europhys. Lett.* **99**, 27001 (2012).
- [41] B. Sothmann, R. Sánchez, A. N. Jordan, and M. Büttiker, *Phys. Rev. B* **85**, 205301 (2012).
- [42] F. Mazza, R. Bosisio, G. Benenti, V. Giovannetti, R. Fazio, and F. Taddei, *New J. Phys.* **16**, 085001 (2014).
- [43] Z. Sartipi and J. Vahedi, *J. Chem. Phys.* **148**, 174302 (2018).
- [44] Z. Sartipi, A. Hayati, and J. Vahedi, *J. Chem. Phys.* **149**, 114103 (2018).
- [45] R. Zhang, Q.-W. Li, F. R. Tang, X. Q. Yang, and L. Bai, *Phys. Rev. E* **96**, 022133 (2017).
- [46] J. Lu, Y. Liu, R. Wang, C. Wang, and J.-H. Jiang, *Phys. Rev. B* **100**, 115438 (2019).
- [47] R. Sánchez, C. Gorini, and G. Fleury, *Phys. Rev. B* **104**, 115430 (2021).
- [48] M. Saha, B. P. Venkatesh, and B. K. Agarwalla, *Phys. Rev. B* **105**, 224204 (2022).
- [49] M. Büttiker, *IBM J. Res. Dev.* **32**, 63 (1988).
- [50] S. Datta, *Quantum Transport: Atom to Transistor* (Cambridge University Press, Cambridge, 2005).